Modeling Water Phenomena in the Cathode Side of Polymer Electrolyte Fuel Cells

Yufan Zhang, [1,2] Gerard Agravante,[3] Thomas Kadyk, [1,4] Michael H. Eikerling [1,2,4] *

1 Theory and Computation of Energy Materials (IEK-13), Institute of Energy and Climate Research, Forschungszentrum Jülich GmbH, 52425 Jülich, Germany

2 Chair of Theory and Computation of Energy Materials, Faculty of Georesources and Materials Engineering, RWTH Aachen University, 52062 Aachen, Germany

3 Department of Chemical and Petroleum Engineering, University of Calgary, T2N 1N4 Calgary, Canada

4 Jülich Aachen Research Alliance, JARA Energy, 52425 Jülich, Germany

** Corresponding author, e-mail: m.eikerling@fz-juelich.de*

ABSTRACT

Water exerts a crucial influence on the performance of a polymer electrolyte fuel cell as both “catalyst activating agent” and “oxygen blocker”. Therefore, fine-tuning the water distribution is imperative for high performance. In this work, we present a water balance model to calculate the distribution of liquid water in cathode catalyst layer and diffusion media. The model incorporates the influence of the local liquid water saturation on the effective transport properties. Liquid water saturation is both a composition variable determining the effective properties, and a solution variable depending on the solution of the transport equations that use the effective properties. The model reveals the formation of a thin water layer in the diffusion medium adjacent to the catalyst layer at high currents. This interfacial water layer strongly impedes oxygen transport and reduces the oxygen concentration in the catalyst layer, which causes the drastic increase of the voltage loss at high currents that drastically reduces the cell performance. We elucidate the origin of the water layer, present parametric studies of this effect, and propose mitigation strategies. The fundamental understanding gained will aid the development of membrane electrode assemblies with tailored pore network properties to achieve vital improvements in performance.

INTRODUCTION

To achieve large-scale commercialization of polymer electrolyte fuel cells (PEFC), performance and durability need to be further improved under the condition of low cost.[1] The cathode catalyst layer (CCL) is vital to cell operation. [2,3] Water inside the CCL plays a dual role.[4–6] On the one hand, it forms proton pathways to reaction sites. Consequently, only the platinum surfaces that are covered by water molecules are rendered electrochemically active. On the other hand, excess liquid water impedes oxygen transport to the reaction sites.[2,7,8]

In between the CCL and the flow field (FF) exist the diffusion media (DM) that bridge the gap of length scales, from nm-sized pores in the CCL to mm-sized channels in the FF).[9] The DM should distribute the gaseous reactants uniformly, provide the electrical connection between the bipolar plates and the CCL, remove water and heat produced in the CCL, and warrant mechanical stability. The DM consist of the gas diffusion layer (GDL) and often the microporous layer (MPL).[10,11] Water management in the DM is of equal, if not higher, importance than in the CCL.[12] A liquid-water volume distribution in the GDL was revealed by x-ray techniques after injecting liquid.[13,14] Continuum theory treated vapor condensation and liquid flow in the GDL and showed water saturation variations.[7] Similar results were obtained using pore network modeling and lattice-Boltzmann simulations.[15,16] A recent theoretical work demonstrated that the drastic voltage loss in the polarization curve in the high current density regime cannot be caused by flooding in the CCL alone, but is rather related to the flooding in the DM.[6] Therefore, the optimal performance of a PEFC hinges on the well-balanced water distribution not only in the CCL but also in the DM.

It is desirable to develop an advanced water balance model that accounts explicitly for the water phenomena in the CCL and the DM. Liquid water saturation, a key variable in our model, should not be treated as a lumped variable within in the CCL or in the DM, but should be treated as a local variable with spatial resolution.[2,6] The local water saturation is then used to calculate the local effective properties, with which the local concentrations and pressures can be obtained by solving continuity equations.[15,17]

We employ macrohomogeneous models (MHM) of CCL and DM.[2,6] The MHM approach assumes that all phases (C, Pt, ionomer, liquid water, gas) coexist in all representative volume elements (RVEs) of the layer with the corresponding physico-chemical properties represented by volume-averages over these RVEs. The MHM for the CCL employs porous electrode theory to describe multi-component transport and electrochemical reactions. The phase-segregated, agglomerated microstructure of the CCL is taken into account by using a bimodal lognormal pore size distribution (PSD) to describe the pore space relevant for water transport. The two peaks in the PSD correspond to primary pores with sizes of 1–10 nm within agglomerates of carbon/Pt and secondary pores with sizes of 10–100 nm between agglomerates. A further explicit consideration of the intra-agglomerate structure, i.e., Pt/C partially covered by ionomer and water, as done e.g. in ref [18] could in principle account for detailed mass transport effects at the agglomerate scale. However, this added model complexity would dramatically increase the model's uncertainty, as the additional parameters are very diverse in the literature and are hard to determine experimentally. [3,18] Hence, our model simplifies these details and focuses on the relevant aspects of the pore network structure.

Our model captures the spatial distribution of the liquid water saturation, effective properties and pressures, helps to pinpoint the culprit of the notorious knee — the voltage loss — seen in polarization curves, and allows exploring parametric effects with low computational cost to optimize the structure and properties of the DM. This model will make a vital contribution to the holistic development of membrane electrode assemblies with customized water management and markedly enhanced performance.

MODEL DEVELOPMENT

Model assumptions and framework

A one-dimensional, isothermal and macro-homogeneous model on the cathode side that consists of the cathode catalyst layer (CCL) and diffusion media (DM) is built, as illustrated in **Figure 1**. The x coordinate points along the through-plane direction and has its origin at the membrane-CCL interface. Oxygen, water vapor, and liquid water are explicitly considered in the system. For simplicity, we assume that no flux of water or oxygen crosses the membrane-CCL interface, which allows us to neglect membrane and anode side in this basic model variant. This assumption can be relaxed at a later stage by introducing fluxes across this interface as parameters or by extending the model by membrane and anode transport models.

Both CCL and DM are spatially resolved, i.e., species pressures, capillary radii, liquid water saturation and effective properties depend on the x coordinate. Proton transport is assumed to be sufficiently rapid so that the potential in CCL is uniform. We consider steady-state processes including the oxygen reduction reaction (ORR) in CCL, vaporization, O_2 and vapor diffusion, and liquid permeation in CCL and DM.

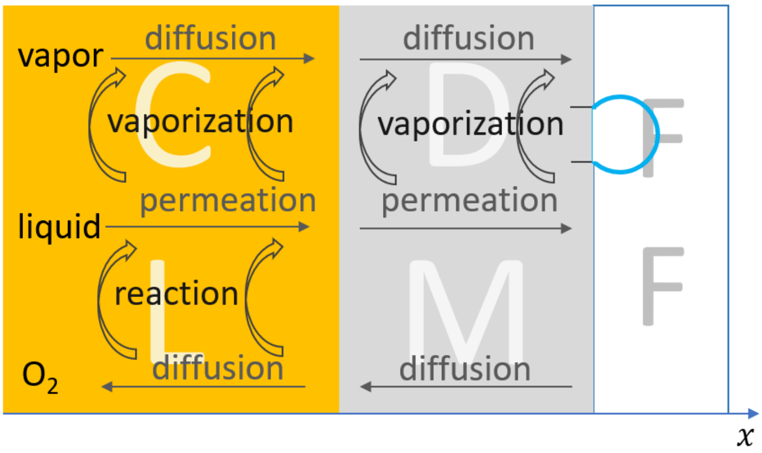

Figure 1. Schematic of the one dimensional, isothermal, and macro-homogeneous model for the cathode side of the membrane electrode assembly (MEA) in a polymer electrolyte fuel cell (PEFC). The considered processes are the oxygen reduction reaction (ORR) in the cathode catalyst layer (CCL), vaporization, O_2 and vapor diffusion, and liquid permeation in CCL and diffusion media (DM).

The liquid water saturation, S_r, plays a central role in this water balance model, and is solved for self-consistently, as illustrated in **Figure 2**. For porous media with known composition and structure, we first use a guess of S_r to obtain effective transport properties by statistical theory of random composite medium.[2] Then, with the effective properties, we can calculate pressures and fluxes using transport equations and continuity equations. Afterwards, using the capillary pressure and the water retention curve, we re-calculate S_r in the next iteration and repeat this loop until convergence of S_r is achieved.

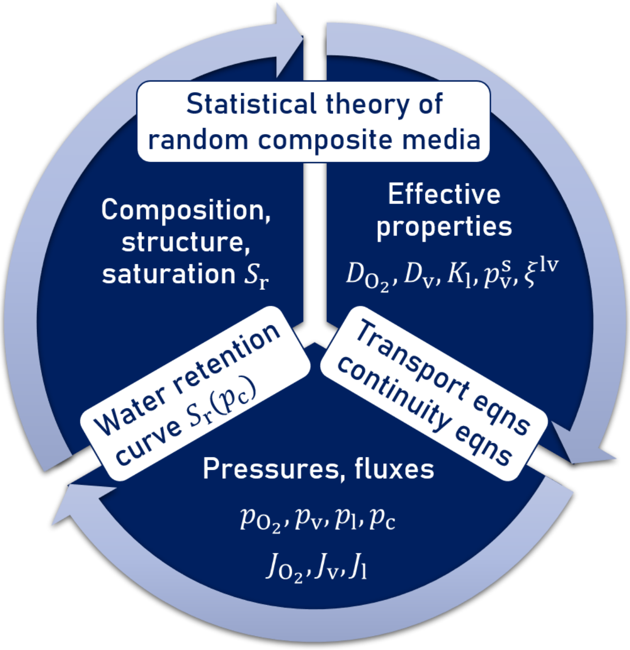

Figure 2. The self-consistent loop for calculating the liquid saturation, S_{r}. It starts with the composition and structure of the porous media. Given an initial guess for S_{r}, effective properties can be calculated with the statistical theory of random composite media. Then, continuity and transport equations are solved for pressure and flux distributions. Having obtained the capillary pressure, S_{r} is re-calculated with the help of water retention curves in the next iteration. The loop is repeated until convergence is achieved.

Pore-size distribution and water retention curve

CCL has mixed wettability.[19] Hydrophilic (HI) pores are characterized by a bimodal log-normal PSD and hydrophobic (HO) pores have a monomodal log-normal PSD. The DM are assumed to have only HO pores with a monomodal log-normal PSD. The PSDs are given by

$$\frac{\mathrm{d}X_{\mathrm{p}}}{\mathrm{d}\ln r}(r) = \begin{cases} \dfrac{X_{\mathrm{p,HI}}}{\sqrt{\pi}\left(\ln s_{\mu} + \chi_{\mathrm{M}} \ln s_{\mathrm{M}}\right)}\left\{\exp\left[-\left(\dfrac{\ln r - \ln r_{\mu}}{\ln s_{\mu}}\right)^{2}\right] + \chi_{\mathrm{CCL}} \exp\left[-\left(\dfrac{\ln r - \ln r_{\mathrm{M}}}{\ln s_{\mathrm{M}}}\right)^{2}\right]\right\}, \text{for CCL HI pores,} \\ \dfrac{X_{\mathrm{p,HO}}}{\sqrt{\pi} \ln s_{\mathrm{HO}}} \exp\left[-\left(\dfrac{\ln r - \ln r_{\mathrm{HO}}}{\ln s_{\mathrm{HO}}}\right)^{2}\right], \text{for CCL HO pores,} \\ \dfrac{X_{\mathrm{p,DM}}}{\sqrt{\pi} \ln s_{\mathrm{DM}}} \exp\left[-\left(\dfrac{\ln r - \ln r_{\mathrm{DM}}}{\ln s_{\mathrm{DM}}}\right)^{2}\right], \text{for DM pores,} \end{cases} \tag{1}$$

where $X_{\mathrm{p,i}}$ (i = HI, HO and DM), r_{j} (j = μ, M, HO and DM) and s_{j} (j = μ, M, HO and DM) stand for the porosity, the mean radius and the standard deviation of the PSD. The μ and M in the subscript denote primary hydrophilic pores and secondary hydrophilic pores in the CCL, respectively. $\chi_{\mathrm{M}} = \frac{X_{\mathrm{p,HI,\mu}}}{X_{\mathrm{p,HI,M}}}$ controls the relative contribution of HI primary and secondary pores where $X_{\mathrm{p,HI,\mu}}$ and $X_{\mathrm{p,HI,M}}$ denote the porosity of primary (inside agglomerate) and secondary (between agglomerate) pores in the CCL.

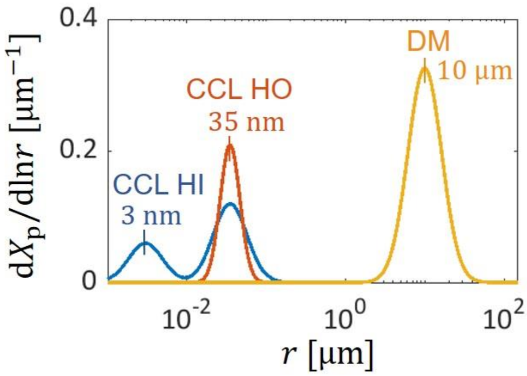

Figure 3. Pore size distributions functions distinguishing between hydrophilic (HI) and hydrophobic (HO) pores in the CCL and pores in the DM. The typical pore size in the DM is three orders magnitude larger than that in the CCL. Parameters used to obtain this figure can be found in the List of parameters in the Appendix.

It is worth noting that the typical pore size in DM is three orders magnitude larger than that in the CL, which exerts a significant impact on water retention curves.

A force balance exists at the liquid-gas interface (see **Figure 4a**). The difference between liquid pressure, p_l, and gas pressure, p_g, is called the capillary pressure, p_c, *viz.* $p_\mathrm{c} = p_\mathrm{l} - p_\mathrm{g}$. Knowing p_c, the capillary radius r_c at any given position x, can be calculated by the Young-Laplace equation,

$$r_\mathrm{c} = -\frac{2\gamma\cos\theta}{p_\mathrm{c}}, \tag{2}$$

with

$$\theta = \begin{cases} \Theta(p_\mathrm{g} - p_\mathrm{l}) \times \theta_\mathrm{HI} + \Theta(p_\mathrm{l} - p_\mathrm{g}) \times \theta_\mathrm{HO}, & \text{for } x \le L_\mathrm{CCL}, \\ \theta_\mathrm{DM}, & \text{for } x > L_\mathrm{CCL}. \end{cases} \tag{3}$$

where $\Theta(y)$ is the Heaviside step function, θ_HI and θ_HO are the contact angles of the HI and HO pores, respectively, and L_CCL is the thickness of CCL.

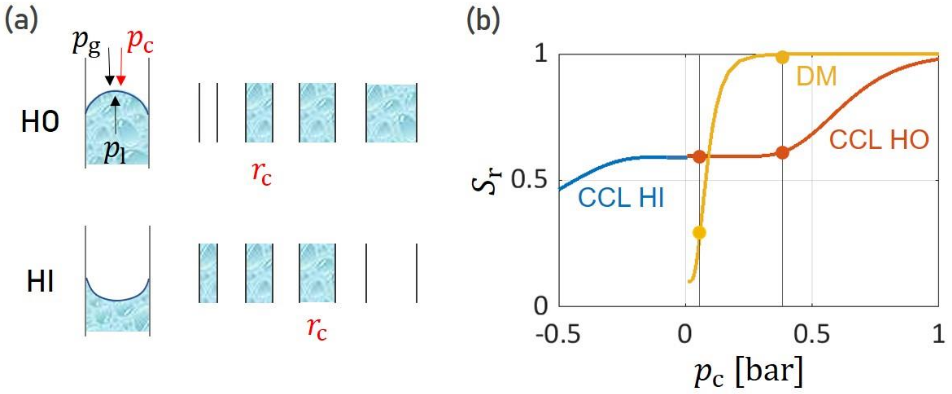

Figure 4. (a) Schematic depiction of the force balance at the liquid-gas interface in hydrophobic (HO) and hydrophilic (HI) pores. For HO pores, the pores larger than r_c are filled with water, whereas for HI pores, the pores smaller than r_c are filled with water. (b) Water retention curves for CCL and DM. The minimal S_r in the DM is set to 0.1 to account for the residual water trapped inside.

In HO pores, all pores with $r > r_\mathrm{c}$ are filled with liquid water, whereas in HI pores, all pores with $r < r_\mathrm{c}$ are filled. The liquid saturation of the different media is obtained by integration over the pore size distribution. For ,

$$S_\mathrm{r}(r_\mathrm{c}) = \begin{cases} \dfrac{1}{X_\mathrm{p,CCL}} \displaystyle\int_{r_\mathrm{min}^\mathrm{HI}}^{r_\mathrm{c}} \mathrm{d}r' \frac{\mathrm{d}X_\mathrm{p,HI}(r')}{\mathrm{d}r'}, & \text{for } x \le L_\mathrm{CCL} \text{ and } p_\mathrm{g} \ge p_\mathrm{l}, \\ \dfrac{1}{X_\mathrm{p,CCL}} \left(\displaystyle\int_{r_\mathrm{min}}^{r_\mathrm{max}^\mathrm{HI}} \mathrm{d}r' \frac{\mathrm{d}X_\mathrm{p,HI}(r')}{\mathrm{d}r'} + \int_{r_\mathrm{c}}^{r_\mathrm{max}^\mathrm{HO}} \mathrm{d}r' \frac{\mathrm{d}X_\mathrm{p,HO}(r')}{\mathrm{d}r'} \right), & \text{for } x \le L_\mathrm{CCL} \text{ and } p_\mathrm{g} < p_\mathrm{l}, \\ 0.1 + \dfrac{0.9}{X_\mathrm{p,DM}} \left(\displaystyle\int_{r_\mathrm{c}}^{r_\mathrm{max}^\mathrm{DM}} \mathrm{d}r' \frac{\mathrm{d}X_\mathrm{p,DM}(r')}{\mathrm{d}r'} \right), & \text{for } x > L_\mathrm{CCL} \end{cases} \tag{4}$$

where $X_\mathrm{p,CCL}$ and $X_\mathrm{p,DM}$ are the porosity of CCL and DM, respectively, $r_\mathrm{min}^\mathrm{HI}$ is the minimal radius for HI pores, $r_\mathrm{max}^\mathrm{k}$ ($\mathrm{k} = \mathrm{HI}, \mathrm{HO}$ and DM) is the maximal radius for HI pores, HO pores in CCL and pores in DM. The expression for $S_\mathrm{r,DM}$ accounts for the hysteresis effect in DM: despite $p_\mathrm{c} = 0$, there is still some liquid water trapped inside DM and hence $S_\mathrm{r,DM} > 0$. Plotting $S_\mathrm{r,CL}$ and $S_\mathrm{r,DM}$ against p_c in Figure 4b, we arrive at the water retention curve, the crucial constitutive relation for porous media. Upon increasing p_c, $S_\mathrm{r,DM}$ increases faster than $S_\mathrm{r,CL}$ and reaches 1 at a much lower p_c, a vital observation that explains water-related performance characteristics of a PEFC.

Effective properties

Effective properties, namely oxygen diffusivity, D_{O_2}, water vapor diffusivity, D_v, liquid water permeability, K_l , saturation vapor pressure, p_v^s, and vaporization interfacial area factor, ξ^lv, are dependent on S_r. Their plots are shown in **Figure 5** and equations for their calculation are given in the Appendix. The exchange current density is assumed to be irrespective of S_r and is estimated to be $5 \times 10^{-3}\ \mathrm{A/m^2}$.

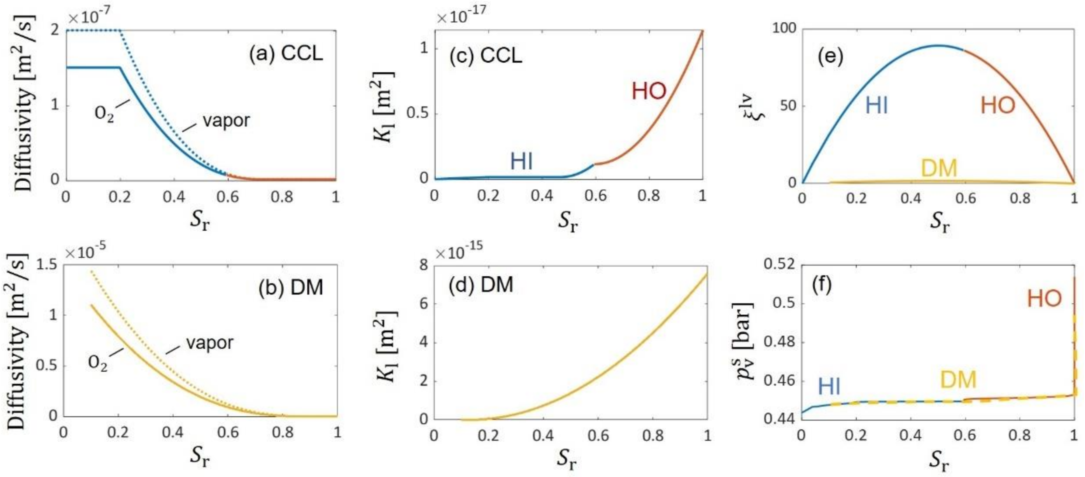

Figure 5. Effective properties as a function of saturation, S_r. (a,b) Diffusivity of oxygen and water vapor in (a) CCL and (b) DM. (c,d) Liquid permeability in (c) CCL and (d) DM. (e) Liquid-air interfacial area factor in CCL and DM. (f) Saturation vapor pressure in CCL and DM.

Governing equations

In porous media, gas transport is described by Fick's law while liquid permeation is described by Darcy's law,

$$J_{\mathrm{O}_2} = -\frac{1}{RT} D_{\mathrm{O}_2} \frac{\mathrm{d}p_{\mathrm{O}_2}}{\mathrm{d}x}, \tag{5}$$

$$J_\mathrm{v} = -\frac{1}{RT} D_\mathrm{v} \frac{\mathrm{d}p_\mathrm{v}}{\mathrm{d}x}, \tag{6}$$

$$J_\mathrm{l} = -\frac{1}{V_\mathrm{m}\mu} K_\mathrm{l} \frac{\mathrm{d}p_\mathrm{l}}{\mathrm{d}x}. \tag{7}$$

where R is gas constant, T is absolute temperature, V_m is molar volume of water, μ is viscosity of water. General form of the continuity equation is

$$\frac{\partial \rho}{\partial t} + \nabla \cdot \boldsymbol{J} = \sigma. \tag{8}$$

where ρ is the density field of the conserved quantity, σ is a source/sink density, and $\boldsymbol{J}$

is a flux density. For a one-dimensional case with steady state, the continuity equations in CCL for oxygen, vapor and liquid water are

$$\frac{\mathrm{d}J_{\mathrm{O_2}}}{\mathrm{d}x} = -\frac{Q_{\mathrm{ORR}}}{4F}, \tag{9}$$

$$\frac{\mathrm{d}J_{\mathrm{v}}}{\mathrm{d}x} = \frac{Q_{\mathrm{lv}}}{2\mathrm{F}}, \tag{10}$$

$$\frac{\mathrm{d}J_{\mathrm{l}}}{\mathrm{d}x} = \frac{Q_{\mathrm{ORR}}}{2F} - \frac{Q_{\mathrm{lv}}}{2\mathrm{F}}. \tag{11}$$

with Q_{ORR} and Q_{lv} being the source terms for ORR and vaporization in units of volumetric current densities, A cm^{-3} and $F = 96485$ as the Faraday constant.

$$Q_{\mathrm{ORR}} = \frac{j^0}{L_{\mathrm{CL}}} \frac{p_{\mathrm{O_2}}}{p_{\mathrm{O_2}}^{\mathrm{ref}}} \exp\left(\frac{\alpha F \eta}{RT}\right), \tag{12}$$

$$Q_{\mathrm{lv}} = \frac{2 e_0 \kappa \xi^{\mathrm{lv}}}{L_{\mathrm{CL}}} (p_{\mathrm{v}}^{\mathrm{s}} - p_{\mathrm{v}}). \tag{13}$$

where $p_{\mathrm{O_2}}^{\mathrm{ref}}$ is the reference pressure of oxygen, α is the transfer coefficient, η is the overpotential, e_0 is the elementary charge, κ is the rate constant of evaporation. The stoichiometry numbers in the cathode reaction $4\mathrm{H}^+ + 4\mathrm{e}^- + \mathrm{O_2} = 2\mathrm{H_2O}$ are $\mathrm{e}^-:\mathrm{O_2}:\mathrm{H_2O} = 4:1:2$, which explains the denominators in Equation (9), (10) and (11). In DM, the continuity equations are,

$$\frac{\mathrm{d}J_{\mathrm{O_2}}}{\mathrm{d}x} = 0, \tag{14}$$

$$\frac{\mathrm{d}J_{\mathrm{v}}}{\mathrm{d}x} = \frac{Q_{\mathrm{lv}}}{2\mathrm{F}}, \tag{15}$$

$$\frac{\mathrm{d}J_{\mathrm{l}}}{\mathrm{d}x} = -\frac{Q_{\mathrm{lv}}}{2\mathrm{F}}. \tag{16}$$

We convert this set of equations into dimensionless form by introducing dimensionless variables summarized in **Table 1**. Each dimensionless variable is obtained by dividing the variable by its corresponding reference value. Feeding a reference capillary radius $r_{\mathrm{c}}^{\mathrm{ref}} = 200$ nm corresponding to CCL HO pores ($p_{\mathrm{g}} < p_{\mathrm{l}}$) into Equation (4), we obtain a reference $S_{\mathrm{r}}^{\mathrm{ref}}$, which can be used to calculate reference effective properties, *viz.* $D_{\mathrm{O_2}}^{\mathrm{ref}}$, $D_{\mathrm{v}}^{\mathrm{ref}}$ and $K_{\mathrm{l}}^{\mathrm{ref}}$. Together with reference pressure, *viz.* $p_{\mathrm{O_2}}^{\mathrm{ref}}$, $p_{\mathrm{v}}^{\mathrm{ref}}$ and $p_{\mathrm{l}}^{\mathrm{s,ref}}$, we can calculate reference fluxes, *viz.* $J_{\mathrm{O_2}}^{\mathrm{ref}}$, $J_{\mathrm{v}}^{\mathrm{ref}}$ and $J_{\mathrm{l}}^{\mathrm{ref}}$,

$$J_{\mathrm{O_2}}^{\mathrm{ref}} = \frac{D_{\mathrm{O_2}}^{\mathrm{ref}}}{RT} \frac{p_{\mathrm{O_2}}^{\mathrm{ref}}}{L_{\mathrm{CL}}}, \tag{17}$$

$$J_{\mathrm{v}}^{\mathrm{ref}} = \frac{D_{\mathrm{v}}^{\mathrm{ref}}}{RT} \frac{p_{\mathrm{v}}^{\mathrm{ref}}}{L_{\mathrm{CL}}}, \tag{18}$$

$$J_{\mathrm{l}}^{\mathrm{ref}} = \frac{K_{\mathrm{l}}^{\mathrm{ref}}}{V\mu} \frac{p_{\mathrm{l}}^{\mathrm{ref}}}{L_{\mathrm{CL}}}. \tag{19}$$

with $p_{\mathrm{v}}^{\mathrm{ref}}$ set to the saturation vapor pressure at flat liquid-gas interface, $p_{\mathrm{v}}^{\mathrm{s},\infty}$, and $p_{\mathrm{O_2}}^{\mathrm{ref}}$ set to the oxygen pressure at the FF inlet.

Table 1. Dimensionless variables used in the domains of both CCL and DM.

Variables	$\tilde{x}$	$\widetilde{p_{\mathrm{O_2}}}$	$\widetilde{J_{\mathrm{O_2}}}$	$\widetilde{p_{\mathrm{v}}}$	$\widetilde{J_{\mathrm{v}}}$	$\widetilde{p_{\mathrm{l}}}$	$\widetilde{J_{\mathrm{l}}}$	$\tilde{r}_{\mathrm{c}}$	$\tilde{\eta}$
Expression	x/L_{CL}	$p_{\mathrm{O_2}}/p_{\mathrm{O_2}}^{\mathrm{ref}}$	$J_{\mathrm{O_2}}/J_{\mathrm{O_2}}^{\mathrm{ref}}$	$p_{\mathrm{v}}/p_{\mathrm{v}}^{\mathrm{ref}}$	$J_{\mathrm{v}}/J_{\mathrm{v}}^{\mathrm{ref}}$	$p_{\mathrm{l}}/p_{\mathrm{l}}^{\mathrm{ref}}$	$J_{\mathrm{l}}/J_{\mathrm{l}}^{\mathrm{ref}}$	$r_{\mathrm{c}}/r_{\mathrm{c}}^{\mathrm{ref}}$	$\alpha F\eta/RT$

Boundary conditions

The model equations and boundary conditions are summarized in **Figure 6**. The left boundary is a gas-tight membrane with zero gas flux across. Also, we assume that the liquid flux across the left boundary is zero.

At the right boundary, *viz.* the DM-FF interface, the boundary conditions for the gas species are their respective pressure at FF inlet.

$$p_{\mathrm{v}}^{\mathrm{in}} = p_{\mathrm{v}}^{\mathrm{s},\infty} \times RH \tag{20}$$

$$p_{\mathrm{O_2}}^{\mathrm{in}} = 0.21 \times (p_{\mathrm{g}}^{\mathrm{in}} - p_{\mathrm{v}}^{\mathrm{in}}) \tag{21}$$

where *RH* is relative humidity.

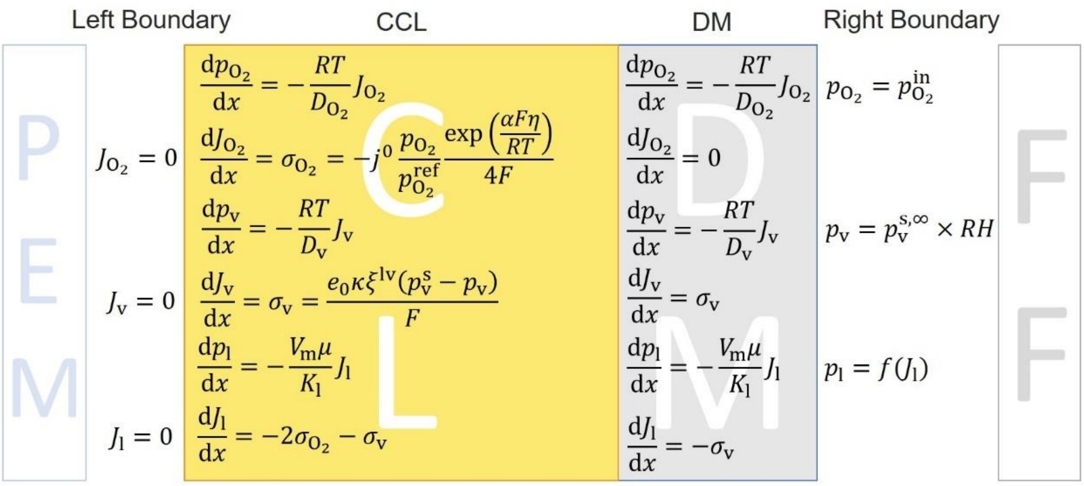

Figure 6. Differential equations and boundary conditions for the domain of cathode catalyst layer and diffusion media.

Specifying the liquid pressure at the right boundary is by no means trivial. In the literature, this pressure was hitherto assumed to be equal to the gas pressure in the FF, *viz.* $p_{\mathrm{l,DM|FF}} = p_{\mathrm{g,FF}}$.[20] However, once a droplet emerges into the FF from a pore opening at the DM surface, the curved droplet surface adds an additional capillary pressure that alters the liquid pressure. As illustrated in **Figure 6**, the liquid pressure at the DM-FF interface depends on J_{l}, and we have developed a simple model to account for this relationship (see the Appendix for details).

RESULTS AND DISCUSSION

In this section, we will first evaluate how the distribution of S_r and effective properties changes with current density using the base-case parameters summarized in **Table 2**. In the base case, DM consist of a GDL but not an MPL.

Table 2. Base-case parameters.

Symbol	Unit	Value
L_CCL	μm	10
L_GDL	μm	90
θ_OH	°	93
θ_DM	°	133
T	K	353
RH	-	1
r_GDL	μm	17.5
p_g^in	bar	1.5
$p_{\mathrm{O}_2}^\mathrm{in}$	bar	0.22

A confined water layer at the GDL side of the CCL-GDL interface

The polarization curve of the base case is shown in **Figure** 7a. A drastic voltage drop occurs at high current densities. In **Figure** 7b, we analyze the S_r distribution for four current densities (j) and observe several key features: (a) S_r in the CL does not change much with j; (b) there is a discontinuity in S_r at the CL-GDL interface; (c) S_r in the GDL increases with j and shows a pronounced peak or "spike" at the interface j, indicating the formation of a confined water layer.

All three features discussed are dictated by the difference of the water retention curves of CCL and GDL. At higher j more liquid water is generated and more oxygen consumed, thus leading to higher p_c. p_c is continuously distributed in the fuel cell and at the CCL-GDL interface. However, the water retention curves of CCL and GDL exhibit distinct behavior (see **Figure 4**b). In the regime of low p_c, S_r in GDL is lower than that in CCL. Increasing p_c, S_r in GDL picks up drastically and asymptotically approaches 1 whereas S_r in CCL does not change much for a wide range of p_c.

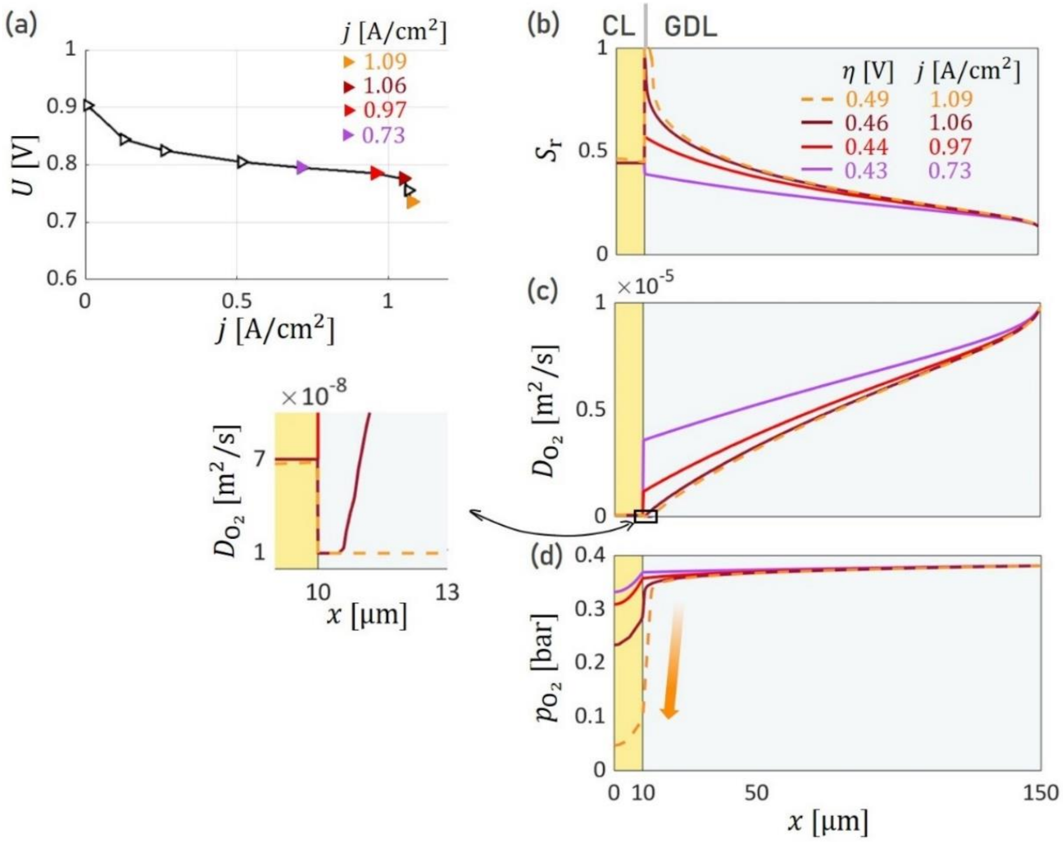

Figure 7. (a) Polarization curve calculated with the basic set of parameters in **Table 2**. For the four colored triangles in (a), 1D distributions of (b) the saturation, (c) the oxygen diffusivity and (d) the oxygen pressure are shown. In (b), (c) and (d), the yellow and grey domains represent the CCL and the GDL, respectively.

At the CL-GDL interface, the increase of S_r leads to a suppression of D_{O_2}. Specifically, the formation of the confined water layer causes an abrupt reduction of D_{O_2} down to a residual diffusivity (see inset in **Figure 4c**). Consequently, $p_{\mathrm{O_2}}$ drops drastically in the DM before oxygen reaches the CCL. Ultimately, this effect leads to the drastic knee-shaped voltage loss typically observed in polarization curves.

Mitigation strategies

Knowing that the confined water layer at the CCL-DM interface is the culprit of the knee-shaped voltage loss, we explore strategies to avoid the build-up of this water layer. The water layer has its root in the water retention curve. In the Young-Laplace equation outlined in Equation (2), the surface tension of the liquid-gas interface is fixed, however, the contact angle and the capillary radius can be controlled. Therefore, we can either tune the wettability of GDL, θ_{GDL}, or tune the PSD of the GDL by shifting the mean pore radius, r_{GDL}. We demonstrate these strategies with the parameter study outlined in **Table 3** and plotted in **Figure 8**.

Table 3 Parameters for the basic case, case 1 and case 2.

Parameter	Basic case	Case 1	Case 2
r_{GDL} [µm]	17.5	10	17.5
θ_{GDL} [°]	133	133	145

As shown in **Figure 8**b, at a given p_{c}, the saturation in the GDL of case 1 and case 2 is lower than that in the base case. This leads to a shift of the knee in the polarization curve to higher current densities, as shown in **Figure 8**c. If we analyze the saturation distribution at an overpotential of 0.45 V in **Figure 8**d, there is no water layer for case 1 and case 2. These results indicate that smaller and more hydrophobic pores in the GDL are beneficial to extend higher current densities operation under “non-flooded” conditions.

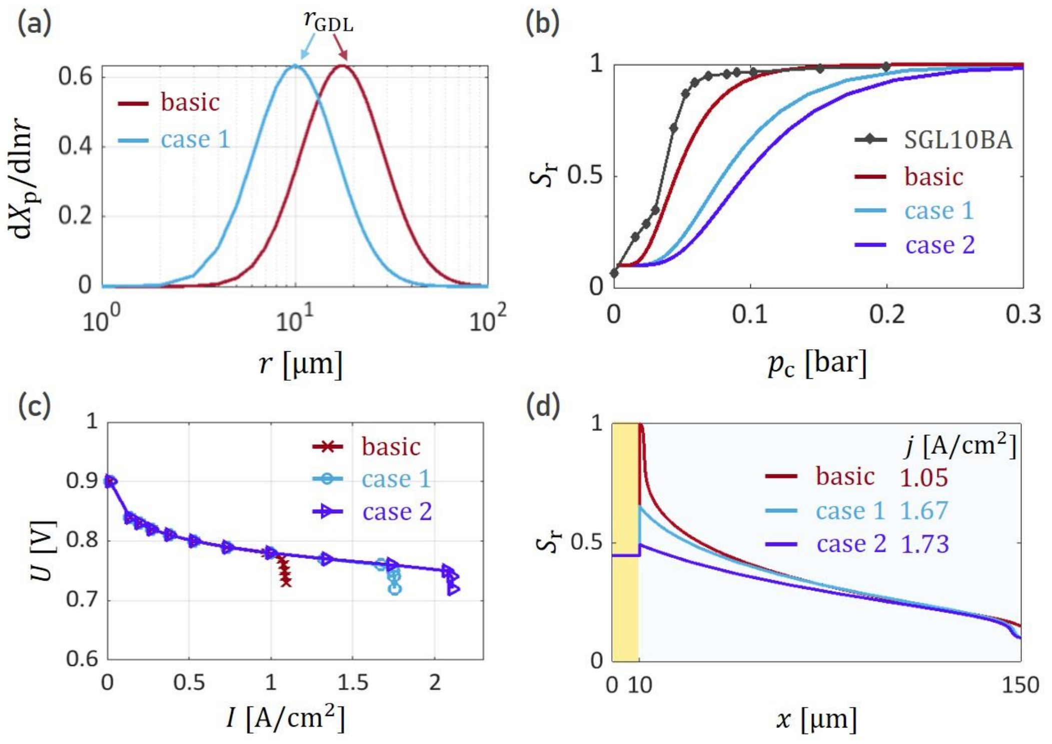

Figure 8. (a) The pore size distribution (PSD) for the basic case and case 1. The peak location is denoted as r_{GDL}. (b) Water retention curves for the base case, case 1 and case 2. The water retention curve of a GDL named SGL10BA is shown as a reference. (c) Polarization curves for the base case, case 1 and case 2. (d) Saturation distribution for the base case, case 1 and case 2 at $\eta = 0.45$ V.

Interestingly, there is a material that features smaller and more hydrophobic pores: the microporous layer. What if we introduce an MPL?

We assume that the MPL has a bimodal log-normal pore size distribution consisting of smaller pores and larger cracks:

$$\frac{\mathrm{d}X_\mathrm{p}}{\mathrm{dln}r}(r) = \frac{X_{\mathrm{p,MPL}}}{\sqrt{\pi}(\ln s_{\mathrm{MPL,p}} + \chi_{\mathrm{MPL}} \ln s_{\mathrm{MPL,crack}})} \left\{ \exp\left[-\left(\frac{\ln r - \ln r_{\mathrm{MPL,p}}}{\ln s_{\mathrm{MPL,p}}} \right)^2 \right] + \chi_{\mathrm{MPL}} \exp\left[-\left(\frac{\ln r - \ln r_{\mathrm{MPL,crack}}}{\ln s_{\mathrm{MPL,crack}}} \right)^2 \right] \right\} \tag{22}$$

We compare three scenarios, namely the DM consisting of i) GDL only, ii) MPL and GDL, and iii) MPL only. The total thickness of the DM is controlled to be 140 µm. For case ii), the thicknesses of the MPL and the GDL are 40 and 100 µm, respectively. The polarization curves in **Figure 9**a show that the performance follows the sequence of case iii > case ii > case i. In other words, using only an MPL reveals the best performance. These phenomena were also observed in experiments conducted by Wang an co-workers (see **Figure 9**b).[8] Notwithstanding this interesting observation, the use of a GDL (in addition to the MPL) is still warranted due to its role in ensuring uniform distributions of the oxygen concentration and flux in the 2D plane interfacing with the CCL.

The reason of this interesting phenomenon is that the contact angle of an MPL is about $155°$, which is higher than the value of $133°$ considered for the GDL, and the typical pore radius of an MPL is around $60\ \mathrm{nm}$, much smaller than that in GDL. The second peak (5 μm) in the PSD of MPL shown in **Figure 9**c denotes cracks. Due to smaller pores and a smaller porosity, at a given saturation the diffusivity in MPL is lower than that in GDL (see **Figure 9**d). However, because of the smaller pores and the more hydrophobic nature, at the same p_c, the saturation in MPL is lower than that in GDL, as is shown in the water retention curves in **Figure 9**e. Now we combine **Figure 9**d and **Figure 9**e to show the diffusivity as a function of capillary pressure in **Figure 9**f. At extremely low p_c, GDL has a higher diffusivity. However, a small increase in p_c will reduce the diffusivity in GDL drastically. This explains why the case with an MPL only for DM exhibits superior performance compared to the other two cases.

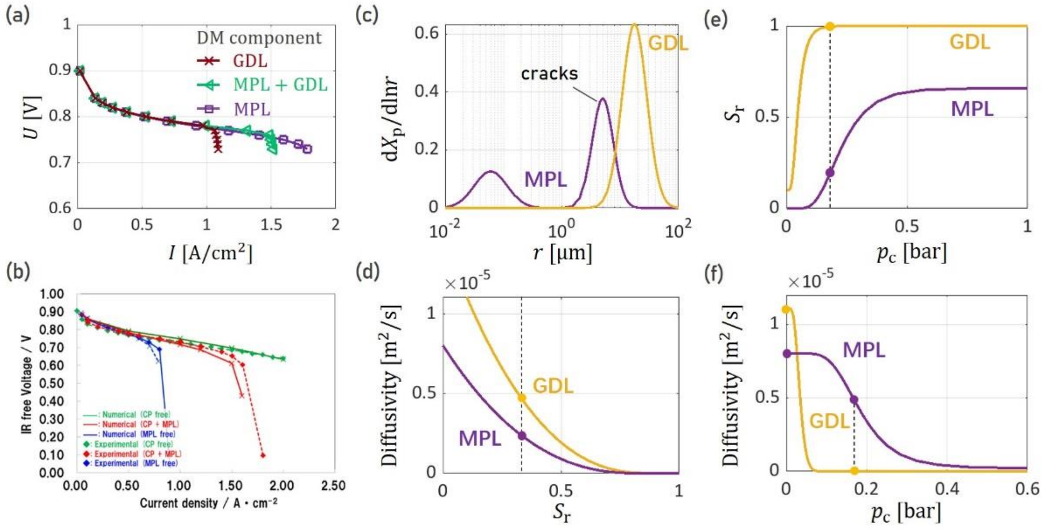

Figure 9. (a) Calculated polarization curves for the case, in which the DM consists of GDL only, GDL plus MPL, and MPL only. (b) Experimental and numerical polarization curves in reference [8]. The DM consist of GDL only (blue), MPL and GDL (red), and MPL only (green).[1] (c) Pore size distributions of MPL and GDL. The MPL follows bimodal log-normal pore size distribution. (d) Oxygen diffusivity as a function of saturation for MPL and GDL. (e) Water retention curves of MPL and GDL. (f) Oxygen diffusivity as a function of capillary pressure for MPL and GDL. Parameters used in this figure can be found in the List of parameters at the end of this article.

It is worth noting that the MPL may intrude into the GDL since the pore radius of the GDL is larger than the MPL particles. [21–24] The intrusion renders the interface of MPL and GDL unsharp, with a transition region from MPL to GDL. The treatment of this intrusion would be more complex and requires detailed experimental characterization. However, since the high current performance has been shown to be sensitive to this interface, a detailed understanding of this intrusion phenomenon would be valuable. We reserve this aspect to future work.

---

[1] Reprinted from Electrochimica Acta, Volume 146, Toshikazu Kotaka, Yuichiro Tabuchi, Ugur Pasaogullari, Chao-Yang Wang, Impact of Interfacial Water Transport in PEMFCs on Cell Performance, 618-629, Copyright (2014), with permission from Elsevier

CONCLUSIONS

In this contribution, we present a water balance model for the PEFC cathode catalyst layer and diffusion media. Our model features a self-consistent treatment of saturation, effective properties and pressure distributions. The saturation, as a key variable, is calculated in a self-consistent manner. Using a starting value of the saturation together with the pore size distribution, the effective properties are obtained using the statistical theory of random composite media. Using the effective properties in continuity equations for oxygen, liquid water and vapor water, pressure distributions of these species are calculated. Then, the saturation distribution is re-calculated and the iterative loop restarts, until convergence is reached.

Our model rationalizes the knee-shape voltage loss typically seen in polarization curves at high current densities by identifying a thin water layer forming in the DM adjacent to the CCL-DM interface. The formation of this confined water layer is due to the continuity of the capillary pressure across the CCL-DM interface with strongly differing water retention curves of CCL and DM. The water layer impedes oxygen transport severely and the oxygen partial pressure drops drastically in DM before oxygen enters into CCL.

A parametric study was performed to explain mitigation strategies. As demonstrated, a more hydrophobic GDL with larger contact angle, as well as a GDL with smaller hydrophobic pores are more desirable. In addition, introducing an MPL into DM elevates the performance, because MPL features smaller and more hydrophobic pores.

ACKNOWLEDGEMENTS

The authors acknowledge funding of the research presented in this article from the Helmholtz-Gemeinschaft Deutscher Forschungszentren e.V. (HGF), Program-oriented Funding (PoF IV), under the Research Program: Materials and Technologies for the Energy Transition (MTET). G.A. acknowledges financial support from DAAD RISE Germany program. Furthermore, we would like to acknowledge fruitful discussions with Wolfgang Olbrich from Bosch GmbH, Lukas Lübben from Volkswagen AG, and Jun Huang from Forschungszentrum Jülich GmbH.

APPENDIX

A1. List of parameters

Symbol	Definition	Value	Ref.
Geometry			
L_{CCL}	Thickness of CCL	10 µm	[2]
L_{DM}	Thickness of DM	140 µm	[8]
L_{MPL}	Thickness of MPL	40 µm	[25]
X_{c}	Percolation threshold	0.1	[26]
X_{el}	Volume fraction of electrolyte	0.3	[27]
X_{PtC}	Volume fraction of solid phase	0.25	[27]
$X_{\mathrm{p,CCL}}$	Volume fraction of pores in CCL	0.45	[2,19]
$X_{\mathrm{p,HI}}$	Volume fraction of total HI pores in CCL	0.2	[19]
$X_{\mathrm{p,HI,\mu}}$	Volume fraction of HI primary pores in CCL	0.067	Assumed
$X_{\mathrm{p,HI,M}}$	Volume fraction of HI secondary pores in CCL	0.133	Assumed
χ_{CCL}	Ratio of HI primary pores to secondary pores	2	[2]
$X_{\mathrm{p,HO}}$	Volume fraction of HO pores in CCL	0.25	[19]
$X_{\mathrm{p,DM}}$	Volume fraction of pores in DM	0.77	[28]
$X_{\mathrm{p,MPL}}$	Volume fraction of total pores in MPL	0.6	[29]
χ_{MPL}	Ratio of MPL pores to cracks	3	[29]
r_{crit}	Critical radius of bottleneck pores in CCL	35 nm	[2]
r_{μ}	Characteristic radius of primary HI pores in	3 nm	[2]

	CCL		
$\boldsymbol{r_{\mathrm{M}}}$	Characteristic radius of secondary HI pores in CCL	35 nm	[2]
$\boldsymbol{r_{\mathrm{HO}}}$	Characteristic radius of HO pores in CCL	35 nm	Assumed
$\boldsymbol{r_{\mathrm{DM}}}$	Characteristic radius of pores in DM	10 μm	[30]
$\boldsymbol{r_{\mathrm{MPL,p}}}$	Characteristic radius of pores in MPL	0.06 μm	[19,30]
$\boldsymbol{r_{\mathrm{MPL,crack}}}$	Radius of the pores corresponding to cracks in MPL	5 μm	[31]
$\boldsymbol{s_{\mu}}$	Standard deviation of PSD of primary HI pores in CCL	2	[2]
$\boldsymbol{s_{\mathrm{M}}}$	Standard deviation of PSD of secondary HO pores in CCL	2	[2]
$\boldsymbol{s_{\mathrm{HO}}}$	Standard deviation of PSD of HO pores in CCL	2	Assumed
$\boldsymbol{s_{\mathrm{DM}}}$	Standard deviation of PSD of pores in DM	2	[2]
$\boldsymbol{s_{\mathrm{MPL,p}}}$	Standard deviation of pores in MPL	2.5	Assumed
$\boldsymbol{s_{\mathrm{MPL,crack}}}$	Standard deviation of the pores corresponding to cracks in MPL	1.8	Assumed
$\boldsymbol{\tau}$	Tortuosity of pores	1.13	[5]
$\boldsymbol{r_{\mathrm{el}}}$	Radius of water-filled pores in ionomer	$1-2$ nm	Assumed
$\boldsymbol{\epsilon_{\mathrm{el}}}$	Relative water volume fraction in ionomer	0.3	[8]
Physical quantities			
$\boldsymbol{D_{\mathrm{res}}}$	Residual diffusivity (in flooded CL and DM)	$1 \times 10^{-8}\ \mathrm{m^2/s}$	Assumed
$\boldsymbol{p_{\mathrm{v}}^{\mathrm{s},\infty}}$	Saturated vapor pressure at 80°C at flat liquid-gas interface	0.45 bar	
$\boldsymbol{\kappa}$	Vaporization rate constant	$1.4 \times 10^{22}\ \mathrm{atm^{-1}m^{-2}s}$	[2]
$\boldsymbol{j_0}$	Exchange current density	$5 \times 10^{-3}\ \mathrm{A/m^2}$	Assumed
$\boldsymbol{\theta_{\mathrm{CCL,HI}}}$	Contact angle of HI pores in CCL	89°	[2]
$\boldsymbol{\theta_{\mathrm{CCL,HO}}}$	Contact angle of HO pores in CCL	93°	[2]
$\boldsymbol{\theta_{\mathrm{GDL}}}$	Contact angle of GDL for the base case	133°	[8,32]
$\boldsymbol{\theta_{\mathrm{MPL}}}$	Contact angle of MPL	155°	[33,34]
$\boldsymbol{\mu_{\mathrm{H_2O}}}$	Viscosity of liquid water	8.9×10^{-4} Pa s	[2]
$\boldsymbol{V_{\mathrm{m}}}$	Molar volume of liquid water	$1.82 \times 10^{-6}\ \mathrm{m^3mol^{-1}}$	
$\boldsymbol{E_{\mathrm{a}}}$	Activation energy for evaporation	0.45 eV	[2]
$\boldsymbol{q_0}$	Pre-exponential factor for calculation of $p_{\mathrm{v}}^{\mathrm{s},\infty}$	1.18×10^{6} atm	[2]
Operating conditions			
$\boldsymbol{p_{\mathrm{O_2}}^{\mathrm{in}}}$	Pressure of inlet oxygen	2 bar	Assumed
$\boldsymbol{T}$	Absolute temperature	353 K	Assumed
$\boldsymbol{RH}$	Relative humidity	100%	Assumed
$\boldsymbol{m_{\mathrm{Pt}}}$	Platinum loading	$0.4\ \mathrm{mg/cm^2}$	Assumed

A2. Equations for calculation of effective properties

Diffusivity

The expression for the diffusivity is described for gas percolation in the open pore space of a partially saturated porous medium. The diffusivity for species i in CCL is given by

$$D_{\mathrm{i}}(S_{\mathrm{r}}) = D_{\mathrm{res}} + D_{0,\mathrm{i}} \frac{1}{(1-X_{\mathrm{c}})^2 (X_{\mathrm{p,CCL}} - X_{\mathrm{c}})^{0.4}} \Big\{ \Theta\big(X_{\mathrm{p,HI,\mu}} - S_{\mathrm{r}} X_{\mathrm{p,CCL}}\big) \big[X_{\mathrm{p,CCL}} - X_{\mathrm{p,HI,\mu}} - X_{\mathrm{c}}\big]^{2.4} + \Theta\big(S_{\mathrm{r}} X_{\mathrm{p,CCL}} - X_{\mathrm{p,HI,\mu}}\big) \Theta\big(X_{\mathrm{p,CCL}} - S_{\mathrm{r}} X_{\mathrm{p,CCL}} - X_{\mathrm{c}}\big) \big[X_{\mathrm{p,CCL}} - S_{\mathrm{r}} X_{\mathrm{p,CCL}} - X_{\mathrm{c}}\big]^{2.4} \Big\}, \tag{A1}$$

with $\Theta(x)$ being the Heaviside function, i being O_2 or v and $D_{0,\mathrm{i}} = \frac{4}{3}\sqrt{\frac{2RT}{\pi M_{\mathrm{i}}}} r_{\mathrm{crit}}$. M_{i} is the molecular weight of species i. Writing Equation (A1) explicitly as a piecewise function, we obtain

$$\begin{aligned}
&\text{for } S_{\mathrm{r}} < \frac{X_{\mathrm{p,HI,\mu}}}{X_{\mathrm{p,CCL}}}, \quad D_{\mathrm{i}}(S_{\mathrm{r}}) = D_{0,\mathrm{i}} \frac{\big[X_{\mathrm{p,CCL}} - X_{\mathrm{p,HI,\mu}} - X_{\mathrm{c}}\big]^{2.4}}{(1-X_{\mathrm{c}})^2 (X_{\mathrm{p,CCL}} - X_{\mathrm{c}})^{0.4}} + D_{\mathrm{res}}, \\
&\text{for } \frac{X_{\mathrm{p,HI,\mu}}}{X_{\mathrm{p,CCL}}} \le S_{\mathrm{r}} < 1 - \frac{X_{\mathrm{c}}}{X_{\mathrm{p,CCL}}}, \quad D_{\mathrm{i}}(S_{\mathrm{r}}) = D_{0,\mathrm{i}} \frac{\big[(1-S_{\mathrm{r}}) X_{\mathrm{p,CCL}} - X_{\mathrm{c}}\big]^{2.4}}{(1-X_{\mathrm{c}})^2 (X_{\mathrm{p,CCL}} - X_{\mathrm{c}})^{0.4}} + D_{\mathrm{res}}, \\
&\text{for } 1 - \frac{X_{\mathrm{c}}}{X_{\mathrm{p,CCL}}} \le S_{\mathrm{r}}, \quad D_{\mathrm{i}}(S_{\mathrm{r}}) = D_{\mathrm{res}},
\end{aligned} \tag{A2}$$

The diffusivity in DM is given by

$$D_{\mathrm{i}}(S_{\mathrm{r}}) = D_{\mathrm{res}} + D_{0,\mathrm{i}} \frac{1}{(1-X_{\mathrm{c}})^2 (X_{\mathrm{p,DM}} - X_{\mathrm{c}})^{0.4}} \Theta\big(X_{\mathrm{p,DM}} - X_{\mathrm{c}} - S_{\mathrm{r,DM}} X_{\mathrm{p,DM}}\big) \big[(1-S_{\mathrm{r}}) X_{\mathrm{p,DM}} - X_{\mathrm{c}}\big]^{2.4}, \tag{A3}$$

and equivalently,

$$\text{for } S_\mathrm{r} < \frac{X_\mathrm{c}}{X_\mathrm{p,DM}}, \qquad D_\mathrm{i}(S_\mathrm{r}) = D_{0,\mathrm{i}} \frac{\left[(1 - S_\mathrm{r})X_\mathrm{p,DM} - X_\mathrm{c}\right]^{2.4}}{(1 - X_\mathrm{c})^2 \left(X_\mathrm{p,DM} - X_\mathrm{c}\right)^{0.4}} + D_\mathrm{res}, \tag{A4}$$

$$\text{for } 1 - \frac{X_\mathrm{c}}{X_\mathrm{p,DM}} \leq S_\mathrm{r}, \qquad D_\mathrm{i}(S_\mathrm{r}) = D_\mathrm{res}.$$

Permeability

The permeability in CCL can be decomposed into four parts, namely permeability due to electrolyte $K_\mathrm{l,el}$, primary HI pores $K_{\mathrm{l,\mu,HI}}$, secondary HI pores $K_\mathrm{l,M,HI}$ and HO pores $K_\mathrm{l,HO}$.

$$K_\mathrm{l}(S_\mathrm{r}) = K_\mathrm{l,el} + K_{\mathrm{l,\mu,HI}} + K_\mathrm{l,M,HI} + K_\mathrm{l,HO}, \tag{A5}$$

$$K_\mathrm{l,el}(S_\mathrm{r}) = 70\delta \frac{r_\mathrm{el}^2}{\tau^2} \epsilon_\mathrm{el} X_\mathrm{el}, \tag{A6}$$

$$K_{\mathrm{l,\mu,HI}}(S_\mathrm{r}) = 70\delta \frac{r_\mu^2}{\tau^2} \left(S_\mathrm{r} X_\mathrm{p} \Theta\left(\frac{X_{\mathrm{\mu,HI}}}{X_\mathrm{p}} - S_\mathrm{r}\right) + X_{\mathrm{\mu,HI}} \Theta\left(S_\mathrm{r} - \frac{X_{\mathrm{\mu,HI}}}{X_\mathrm{p}}\right)\right), \tag{A7}$$

$$\begin{aligned} K_\mathrm{l,M,HI}(S_\mathrm{r}) = 70\delta r_\mathrm{M}^2 \Bigg(& \frac{\left[S_\mathrm{r} X_\mathrm{p} - X_{\mathrm{\mu,HI}} - X_\mathrm{c}\right]^2}{(1 - X_\mathrm{c})^2} \Theta\Bigg(S_\mathrm{r} \\ & - \frac{X_{\mathrm{\mu,HI}} + X_\mathrm{c}}{X_\mathrm{p}}\Bigg) \Theta\left(\frac{X_\mathrm{p,HI}}{X_\mathrm{p}} - S_\mathrm{r}\right) \\ & + \frac{\left[X_\mathrm{p,HI} - X_{\mathrm{\mu,HI}} - X_\mathrm{c}\right]^2}{(1 - X_\mathrm{c})^2} \Theta\left(S_\mathrm{r} - \frac{X_\mathrm{p,HI}}{X_\mathrm{p}}\right)\Bigg), \end{aligned} \tag{A8}$$

$$K_\mathrm{l,HO}(S_\mathrm{r}) = 70\delta r_\mathrm{HO}^2 \frac{(S_\mathrm{r} X_\mathrm{p} - X_\mathrm{p,HI})^2}{(1 - X_\mathrm{c})^2} \Theta\left(S_\mathrm{r} - \frac{X_\mathrm{p,HI}}{X_\mathrm{p}}\right). \tag{A9}$$

The piecewise representation of K_l is

$$
\begin{aligned}
&\text{for } S_{\mathrm{r}} < \frac{X_{\mu,\mathrm{HI}}}{X_{\mathrm{p,CCL}}}, \quad K_{\mathrm{l}}(S_r) = 70\delta\left\{\frac{r_{\mathrm{el}}^2}{\tau^2}\epsilon_{\mathrm{el}}X_{\mathrm{el}} + \frac{r_{\mu}^2}{\tau^2}S_{\mathrm{r}}X_{\mathrm{p,CCL}}\right\},\\
&\text{for } \frac{X_{\mu,\mathrm{HI}}}{X_{\mathrm{p,CCL}}} \le S_{\mathrm{r}} < \frac{X_{\mu,\mathrm{HI}} + X_{\mathrm{c}}}{X_{\mathrm{p,CCL}}}, \qquad K_{\mathrm{l}}(S_r) = 70\delta\left\{\frac{r_{\mathrm{el}}^2}{\tau^2}\epsilon_{\mathrm{el}}X_{\mathrm{el}} + \frac{r_{\mu}^2}{\tau^2}X_{\mu,\mathrm{HI}}\right\},\\
&\text{for } \frac{X_{\mu,\mathrm{HI}} + X_{\mathrm{c}}}{X_{\mathrm{p,CCL}}} \le S_{\mathrm{r}} < \frac{X_{\mathrm{p,HI}}}{X_{\mathrm{p,CCL}}}, \quad K_{\mathrm{l}}(S_r)\\
&\qquad = 70\delta\left\{\frac{r_{\mathrm{el}}^2}{\tau^2}\epsilon_{\mathrm{el}}X_{\mathrm{el}} + \frac{r_{\mu}^2}{\tau^2}X_{\mu} + r_{\mathrm{M}}^2\frac{\left[S_{\mathrm{r}}X_{\mathrm{p,CCL}} - X_{\mu,\mathrm{HI}} - X_{\mathrm{c}}\right]^2}{(1-X_{\mathrm{c}})^2}\right\},\\
&\text{for } S_{\mathrm{r}} \ge \frac{X_{\mathrm{p,HI}}}{X_{\mathrm{p,CCL}}}, \quad K_{\mathrm{l}}(S_{\mathrm{r}})\\
&\qquad = 70\delta\left\{\frac{r_{\mathrm{el}}^2}{\tau^2}\epsilon_{\mathrm{el}}X_{\mathrm{el}} + \frac{r_{\mu}^2}{\tau^2}X_{\mu} + r_{\mathrm{M}}^2\frac{\left[X_{\mathrm{p,HI}} - X_{\mu,\mathrm{HI}} - X_{\mathrm{c}}\right]^2}{(1-X_{\mathrm{c}})^2}\right.\\
&\qquad \left. + r_{\mathrm{HO}}^2\frac{\left(S_{\mathrm{r}}X_{\mathrm{p,CCL}} - X_{\mathrm{p,HI}}\right)^2}{(1-X_{\mathrm{c}})^2}\right\}.
\end{aligned}
\tag{A10}
$$

In DM, the permeability is given by

$$
K_{\mathrm{l}}(S_{\mathrm{r}}) = K_{\mathrm{res}} + \Theta\left(S_{\mathrm{r}}X_{\mathrm{p,DM}} - X_{\mathrm{c}}\right)\frac{\delta_{\mathrm{DM}}r_{\mathrm{DM}}^2}{0.2}\frac{\left[S_{\mathrm{r}}X_{\mathrm{p,DM}} - X_{\mathrm{c}}\right]^2}{(1-X_{\mathrm{c}})^2},
\tag{A11}
$$

and equivalently

$$
\begin{aligned}
&\text{for } S_{\mathrm{r}} < \frac{X_{\mathrm{c}}}{X_{\mathrm{p,DM}}}, \quad K_{\mathrm{l}}(S_{\mathrm{r}}) = K_{\mathrm{res}},\\
&\text{for } \frac{X_{\mathrm{c}}}{X_{\mathrm{p,DM}}} \le S_{\mathrm{r}}, \qquad K_{\mathrm{l}}(S_{\mathrm{r}}) = K_{\mathrm{res}} + \frac{\delta_{\mathrm{DM}}r_{\mathrm{DM}}^2}{0.2}\frac{\left[S_{\mathrm{r}}X_{\mathrm{p,DM}} - X_{\mathrm{c}}\right]^2}{(1-X_{\mathrm{c}})^2}.
\end{aligned}
\tag{A12}
$$

Liquid/vapor interfacial area factor

The liquid-vapor interfacial area factor (ξ^{lv}) is a dimensionless quantity that determines the vaporization rate. ξ^{lv} is zero either when the porous media is fully dry or saturated. ξ^{lv} reaches the maximal value when $S_{\mathrm{r}} = 0.5$.

$$\text{for CCL}, \xi^{\mathrm{lv}} = L_{\mathrm{CCL}} S_{\mathrm{r}} (1 - S_{\mathrm{r}}) \int_{r_{\mathrm{CCL}}^{\min}}^{r_{\mathrm{CCL}}^{\max}} \left(\frac{\mathrm{d}X_{\mathrm{p,HI}}}{\mathrm{d}r} + \frac{\mathrm{d}X_{\mathrm{p,HO}}}{\mathrm{d}r} \right) \frac{1}{r'} \mathrm{d}r', \tag{A13}$$

$$\text{for DM}, \xi^{\mathrm{lv}} = L_{\mathrm{DM}} S_{\mathrm{r}} (1 - S_{\mathrm{r}}) \int_{r_{\mathrm{DM}}^{\min}}^{r_{\mathrm{DM}}^{\max}} \frac{\mathrm{d}X_{\mathrm{p,DM}}}{\mathrm{d}r} \frac{1}{r'} \mathrm{d}r'.$$

A more complicated expression for ξ^{lv} can be found in Ref [19].

Saturation vapor pressure

The saturation vapor pressure on top of a curved vapor-liquid interface is written as

$$\text{for CCL}, \tag{A14}$$

$$p_{\mathrm{v}}^{\mathrm{s}} = p_{\mathrm{v}}^{\mathrm{s},\infty} \exp\left(-\frac{2\gamma V_{\mathrm{m}} \cos\left(\theta_{\mathrm{HI}} \Theta(p_{\mathrm{g}} - p_{\mathrm{l}}) + \theta_{\mathrm{HO}} \Theta(p_{\mathrm{l}} - p_{\mathrm{g}})\right)}{R T r_{\mathrm{c}}} \right),$$

$$\text{for DM}, \qquad p_{\mathrm{v}}^{\mathrm{s}} = p_{\mathrm{v}}^{\mathrm{s},\infty} \exp\left(-\frac{2\gamma V_{\mathrm{m}} \cos\theta_{\mathrm{DM}}}{R T r_{\mathrm{c}}} \right).$$

with the molar volume of liquid V_{m} and the saturation vapor pressure for planar vapor-liquid interface $p_{\mathrm{v}}^{\mathrm{s},\infty} = q^0 \exp\left(-\frac{E_{\mathrm{a}}}{k_{\mathrm{B}} T}\right)$. Here, q^0 is a pre-exponential factor and E_{a} is an activation energy of evaporation.

A3. Boundary condition for the transport equation of liquid in the bulk DM

In our model, the bulk DM is separated from the FF not by an interface with zero thickness, but by a domain of thickness l that accommodates a bundle of pores, following the description first proposed by Baber et al.[35,36] The domain consists of cylindrical pores of different radii r_i $(i = 1, 2, \dots N)$. The entrances (openings on the left) of the pores connect to the rest of the DM while the exits (openings on the right) connect to the FF. The pores are connected only at the pore entrances and the liquid pressure therein, $p_{\mathrm{l,pe}}$, is assumed to be the same for all pore entrances. The boundary of the transport equations in the bulk DM is set to the plane of the pore entrances of the bundle-of-pores domain. The boundary condition is therefore the liquid pressure at the pore entrances, $p_{\mathrm{l,pe}}$.

We approximate the PSD of the bundle-of-pore domain by a lognormal distribution confined within an interval of a minimal pore radius r_{min} and a maximal pore radius r_{max}, as described in

$$\frac{\mathrm{d}X_{\mathrm{p}}^{\mathrm{surf}}}{\mathrm{d}r} = \frac{\frac{1}{r}\frac{1}{\sqrt{\pi}\ln s}\exp\left[-\left(\frac{\ln r - \ln r_{\mathrm{mean}}}{\ln s}\right)^{2}\right]}{\int_{r_{\mathrm{min}}}^{r_{\mathrm{max}}}\frac{1}{r}\frac{1}{\sqrt{\pi}\ln s}\exp\left[-\left(\frac{\ln r - \ln r_{\mathrm{mean}}}{\ln s}\right)^{2}\right]\mathrm{d}r}, \tag{A15}$$

with r_{mean} and s being the mean value and standard deviation of the lognormal distribution. The PSD in (A15) is normalized, i.e., $\int_{r_{\mathrm{min}}}^{r_{\mathrm{max}}}\frac{\mathrm{d}X_{\mathrm{p}}^{\mathrm{surf}}}{\mathrm{d}r}\mathrm{d}r = 1$.

For a certain amount of liquid flowing into this domain, only a certain fraction of pores allows for liquid expulsion. We term these pores the activated pores. Activation of a specific pore is possible if $p_{\mathrm{l,pe}}$ is higher than the liquid pressure at the pore exit. For the pore of radius r, the liquid pressure at the pore exit is termed the threshold pressure and is calculated by

$$p_{\mathrm{l,th}} = p_{\mathrm{g,FF}} + \frac{2\gamma}{r}. \tag{A16}$$

Just as the name “threshold pressure” indicates, once $p_{\mathrm{l,pe}}$ is larger than $p_{\mathrm{l,th}}$, liquid is able to transport through the pore of radius r. It is obvious that the pore with the largest r has the lowest $p_{\mathrm{l,th}}$ and, thus, is the easiest to be activated. Therefore, the activation of pores will start from the largest pore to smaller and smaller pores. The radius of the smallest activated pore is denoted as r_{low}.

For DM surface with area $S_{\mathrm{DM}}^{\mathrm{surf}}$, we use $N_{\mathrm{p}}^{\mathrm{surf}}$ to denote the total number of pores on the surface. The area-specific number density of pores is then $n_{\mathrm{p}}^{\mathrm{surf}} = N_{\mathrm{p}}^{\mathrm{surf}}/S_{\mathrm{DM}}^{\mathrm{surf}}$. The total area of pores ($S_\mathrm{p}^\mathrm{surf}$) can be expressed by a sum of pore area of all the pores

$$S_\mathrm{p}^\mathrm{surf} = N_\mathrm{p}^\mathrm{surf} \int_{r_\mathrm{min}}^{r_\mathrm{max}} \frac{\mathrm{d}X_\mathrm{p}^\mathrm{surf}}{\mathrm{d}r} \pi r^2 \,\mathrm{d}r. \tag{A17}$$

The area fraction of the total pores to the DM surface can be expressed by $X_\mathrm{p}^\mathrm{surf} = S_\mathrm{p}^\mathrm{surf}/S_\mathrm{DM}^\mathrm{surf}$. Dividing $S_\mathrm{DM}^\mathrm{surf}$ on both sides of Equation (A17) and writing $n_\mathrm{p}^\mathrm{surf}$ on the left-hand side, we have

$$n_\mathrm{p}^\mathrm{surf} = \frac{X_\mathrm{p}^\mathrm{surf}}{\int_{r_\mathrm{min}}^{r_\mathrm{max}} \frac{\mathrm{d}X_\mathrm{p}^\mathrm{surf}}{\mathrm{d}r} \pi r^2 \,\mathrm{d}r}. \tag{A18}$$

From top-view SEM images on the DM surface, $S_\mathrm{p}^\mathrm{surf}$ and $S_\mathrm{DM}^\mathrm{surf}$ can be obtained, and then $X_\mathrm{p}^\mathrm{surf}$ can be calculated. To the first approximation, $\frac{\mathrm{d}X_\mathrm{p}^\mathrm{surf}}{\mathrm{d}r}$ can be taken as the value in the bulk, which can be measured by mercury intrusion experiment. Then, $n_\mathrm{p}^\mathrm{surf}$ is readily calculated by Equation (A18).

J_l is the liquid flux from the bulk DM into the bundle-of-pores domain. With the assumption of no vaporization in the domain, J_l is equal to the liquid flux through all the activated pores. Thus, J_l is expressed as an integral over the fluxes through all activated pores,

$$J_\mathrm{l} = n_\mathrm{p}^\mathrm{surf} \int_{r_\mathrm{low}}^{r_\mathrm{max}} \frac{\mathrm{d}X_\mathrm{p}^\mathrm{surf}}{\mathrm{d}r} J_\mathrm{p}\,(r) \mathrm{d}r, \tag{A19}$$

with J_p being the liquid flux through a pore of radius r, described by the Hagen-Poiseuille law,

$$J_\mathrm{p}(r) = \frac{\rho}{8\mu l} r^2 \left(p_\mathrm{l,pe} - p_\mathrm{l,th}\,(r)\right), \tag{A20}$$

Since r_{low} is the radius of the pore that is just activated, the liquid pressure at the entrance should be equal to the threshold pressure at the exit,

$$p_{\mathrm{l,pe}} = p_{\mathrm{l,th}}(r_{\mathrm{low}}) = p_{\mathrm{g,FF}} + \frac{2\gamma}{r_{\mathrm{low}}}. \tag{A21}$$

Combining Equations (A19)-(A21), we arrive at the final equation to solve for r_{low},

$$J_{\mathrm{l}} = \frac{n_{\mathrm{p}}^{\mathrm{surf}}\rho}{8\mu l}\int_{r_{\mathrm{low}}}^{r_{\mathrm{max}}} \frac{\mathrm{d}X_{\mathrm{p}}^{\mathrm{surf}}}{\mathrm{d}r}\,\pi r^4\,2\gamma\left(\frac{1}{r_{\mathrm{low}}} - \frac{1}{r}\right)\mathrm{d}r. \tag{A22}$$

This equation is nonlinear in r_{low}, so numerical solution is warranted. Substituting the obtained r_{low} back to Equation (A21) gives the boundary condition for liquid pressure, $p_{\mathrm{l,pe}}$.

REFERENCES

[1] Y. Wang, Y. Pang, H. Xu, A. Martinez, K.S. Chen, PEM Fuel cell and electrolysis cell technologies and hydrogen infrastructure development – a review, Energy Environ. Sci. 15 (2022) 2288–2328. https://doi.org/10.1039/D2EE00790H.

[2] M. Eikerling, Water Management in Cathode Catalyst Layers of PEM Fuel Cells, Journal of The Electrochemical Society. 153 (2006) E58. https://doi.org/10.1149/1.2160435.

[3] J. Huang, Z. Li, J. Zhang, Review of characterization and modeling of polymer electrolyte fuel cell catalyst layer: The blessing and curse of ionomer, Frontiers in Energy. 11 (2017) 334–364. https://doi.org/10.1007/s11708-017-0490-6.

[4] W. Olbrich, T. Kadyk, U. Sauter, M. Eikerling, Review—Wetting Phenomena in Catalyst Layers of PEM Fuel Cells: Novel Approaches for Modeling and Materials Research, Journal of The Electrochemical Society. 169 (2022) 054521. https://doi.org/10.1149/1945-7111/ac6e8b.

[5] T. Muzaffar, T. Kadyk, M. Eikerling, Tipping water balance and the Pt loading effect in

polymer electrolyte fuel cells: a model-based analysis, Sustainable Energy Fuels. 2 (2018) 1189–1196. https://doi.org/10.1039/C8SE00026C.

[6] J. Liu, M. Eikerling, Model of cathode catalyst layers for polymer electrolyte fuel cells: The role of porous structure and water accumulation, Electrochimica Acta. 53 (2008) 4435–4446. https://doi.org/10.1016/j.electacta.2008.01.033.

[7] J.H. Nam, M. Kaviany, Effective diffusivity and water-saturation distribution in single- and two-layer PEMFC diffusion medium, International Journal of Heat and Mass Transfer. 46 (2003) 4595–4611. https://doi.org/10.1016/S0017-9310(03)00305-3.

[8] T. Kotaka, Y. Tabuchi, U. Pasaogullari, C.-Y. Wang, Impact of Interfacial Water Transport in PEMFCs on Cell Performance, Electrochimica Acta. 146 (2014) 618–629. https://doi.org/10.1016/j.electacta.2014.08.148.

[9] Q. Chen, Z. Niu, H. Li, K. Jiao, Y. Wang, Recent progress of gas diffusion layer in proton exchange membrane fuel cell: Two-phase flow and material properties, International Journal of Hydrogen Energy. 46 (2021) 8640–8671. https://doi.org/10.1016/j.ijhydene.2020.12.076.

[10] M. Göbel, M. Godehardt, K. Schladitz, Multi-scale structural analysis of gas diffusion layers, Journal of Power Sources. 355 (2017) 8–17. https://doi.org/10.1016/j.jpowsour.2017.03.086.

[11] H.P.F. Gunterman, Characterization of Fuel-Cell Diffusion Media., UC Berkeley, 2011.

[12] K. Chan, M. Eikerling, Water balance model for polymer electrolyte fuel cells with ultrathin catalyst layers, Phys. Chem. Chem. Phys. 16 (2014) 2106–2117. https://doi.org/10.1039/C3CP54849J.

[13] M. Sabharwal, J.T. Gostick, M. Secanell, Virtual Liquid Water Intrusion in Fuel Cell Gas Diffusion Media, Journal of The Electrochemical Society. 165 (2018) F553–F563. https://doi.org/10.1149/2.0921807jes.

[14] A. Mularczyk, Q. Lin, M.J. Blunt, A. Lamibrac, F. Marone, T.J. Schmidt, F.N. Büchi, J.

Eller, Droplet and Percolation Network Interactions in a Fuel Cell Gas Diffusion Layer, Journal of The Electrochemical Society. 167 (2020) 084506. https://doi.org/10.1149/1945-7111/ab8c85.

[15] I.V. Zenyuk, E. Medici, J. Allen, A.Z. Weber, Coupling continuum and pore-network models for polymer-electrolyte fuel cells, International Journal of Hydrogen Energy. 40 (2015) 16831–16845. https://doi.org/10.1016/j.ijhydene.2015.08.009.

[16] D.H. Jeon, Effect of channel-rib width on water transport behavior in gas diffusion layer of polymer electrolyte membrane fuel cells, Journal of Power Sources. 423 (2019) 280–289. https://doi.org/10.1016/j.jpowsour.2019.03.079.

[17] P.A. García-Salaberri, J.T. Gostick, G. Hwang, A.Z. Weber, M. Vera, Effective diffusivity in partially-saturated carbon-fiber gas diffusion layers: Effect of local saturation and application to macroscopic continuum models, Journal of Power Sources. 296 (2015) 440–453. https://doi.org/10.1016/j.jpowsour.2015.07.034.

[18] W. Olbrich, T. Kadyk, U. Sauter, M. Eikerling, Modeling of wetting phenomena in cathode catalyst layers for PEM fuel cells, Electrochimica Acta. 431 (2022) 140850. https://doi.org/10.1016/j.electacta.2022.140850.

[19] J. Zhou, A. Putz, M. Secanell, A Mixed Wettability Pore Size Distribution Based Mathematical Model for Analyzing Two-Phase Flow in Porous Electrodes, Journal of The Electrochemical Society. 164 (2017) F530–F539. https://doi.org/10.1149/2.0381706jes.

[20] A.Z. Weber, J. Newman, Modeling Transport in Polymer-Electrolyte Fuel Cells, Chem. Rev. 104 (2004) 4679–4726. https://doi.org/10.1021/cr020729l.

[21] J. Gostick, M. Fowler, M. Ioannidis, M. Pritzker, Y. Vol’fkovich, A. Sakars, Capillary pressure and hydrophilic porosity in gas diffusion layers for polymer electrolyte fuel cells, Journal of Power Sources. 156 (2006) 375–387. https://doi.org/10.1016/j.jpowsour.2005.05.086.

[22] A. Lamibrac, J. Roth, M. Toulec, F. Marone, M. Stampanoni, F.N. Büchi, Characterization

of Liquid Water Saturation in Gas Diffusion Layers by X-Ray Tomographic Microscopy, Journal of The Electrochemical Society. 163 (2015) F202. https://doi.org/10.1149/2.0401603jes.

[23] Z. Fishman, A. Bazylak, Heterogeneous Through-Plane Porosity Distributions for Treated PEMFC GDLs. II. Effect of MPL Cracks, Journal of The Electrochemical Society. 158 (2011) B846. https://doi.org/10.1149/1.3594636.

[24] R.W.I. Atkinson, Y. Garsany, B.D. Gould, K.E. Swider-Lyons, I.V. Zenyuk, The Role of Compressive Stress on Gas Diffusion Media Morphology and Fuel Cell Performance, ACS Appl. Energy Mater. 1 (2018) 191–201. https://doi.org/10.1021/acsaem.7b00077.

[25] J. Lee, R. Yip, P. Antonacci, N. Ge, T. Kotaka, Y. Tabuchi, A. Bazylak, Synchrotron Investigation of Microporous Layer Thickness on Liquid Water Distribution in a PEM Fuel Cell, Journal of The Electrochemical Society. 162 (2015) F669. https://doi.org/10.1149/2.0221507jes.

[26] M. Eikerling, A. Kornyshev, A. Kulikovsky, Encyclopedia of Electrochemistry, Wiley-VCH, Weinheim, n.d.

[27] Q. Wang, M. Eikerling, D. Song, Z. Liu, T. Navessin, Z. Xie, S. Holdcroft, Functionally Graded Cathode Catalyst Layers for Polymer Electrolyte Fuel Cells: I. Theoretical Modeling, Journal of The Electrochemical Society. 151 (2004) A950. https://doi.org/10.1149/1.1753580.

[28] R. Flückiger, F. Marone, M. Stampanoni, A. Wokaun, F.N. Büchi, Investigation of liquid water in gas diffusion layers of polymer electrolyte fuel cells using X-ray tomographic microscopy, Electrochimica Acta. 56 (2011) 2254–2262. https://doi.org/10.1016/j.electacta.2010.12.016.

[29] Y.-C. Chen, C. Karageorgiou, J. Eller, T.J. Schmidt, F.N. Büchi, Determination of the porosity and its heterogeneity of fuel cell microporous layers by X-ray tomographic microscopy, Journal of Power Sources. 539 (2022) 231612. https://doi.org/10.1016/j.jpowsour.2022.231612.

[30] H. Ostadi, P. Rama, Y. Liu, R. Chen, X.X. Zhang, K. Jiang, 3D reconstruction of a gas diffusion layer and a microporous layer, Journal of Membrane Science. 351 (2010) 69–74.

https://doi.org/10.1016/j.memsci.2010.01.031.

[31] C.-J. Tseng, S.-K. Lo, Effects of microstructure characteristics of gas diffusion layer and microporous layer on the performance of PEMFC, Energy Conversion and Management. 51 (2010) 677–684. https://doi.org/10.1016/j.enconman.2009.11.011.

[32] A. Theodorakakos, T. Ous, M. Gavaises, J.M. Nouri, N. Nikolopoulos, H. Yanagihara, Dynamics of water droplets detached from porous surfaces of relevance to PEM fuel cells, Journal of Colloid and Interface Science. 300 (2006) 673–687. https://doi.org/10.1016/j.jcis.2006.04.021.

[33] P. Gallo Stampino, C. Cristiani, G. Dotelli, L. Omati, L. Zampori, R. Pelosato, M. Guilizzoni, Effect of different substrates, inks composition and rheology on coating deposition of microporous layer (MPL) for PEM-FCs, Catalysis Today. 147 (2009) S30–S35. https://doi.org/10.1016/j.cattod.2009.07.023.

[34] S. Latorrata, P. Gallo Stampino, C. Cristiani, G. Dotelli, Novel superhydrophobic microporous layers for enhanced performance and efficient water management in PEM fuel cells, International Journal of Hydrogen Energy. 39 (2014) 5350–5357. https://doi.org/10.1016/j.ijhydene.2013.12.199.

[35] K. Baber, Coupling free flow and flow in porous media in biological and technical applications : from a simple to a complex interface description, dissertation, Universität Stuttgart, 2014.

[36] K. Baber, B. Flemisch, R. Helmig, Modeling drop dynamics at the interface between free and porous-medium flow using the mortar method, International Journal of Heat and Mass Transfer. 99 (2016) 660–671. https://doi.org/10.1016/j.ijheatmasstransfer.2016.04.014.